The role of water in promoting cooperative interactions between amine and grafted Sn or Ti Sites on silica

Christine Khoury,[†] *Samuel Holton,*[§] *Dina Shpasser,*[†] *Elior Hallo,*[†] *Ambarish Kulkarni,*[§] *Friederike C. Jentoft**[‡] *and Oz M. Gazit*[†]**

[†] Wolfson Faculty of Chemical Engineering, Technion – Israel Institute of Technology, Haifa, Israel, 3200003.

[§] Department of Chemical Engineering, University of California Davis, Davis, California, USA, 95618.

[‡] Department of Chemical Engineering, University of Massachusetts Amherst, Amherst, MA, USA, 01003-9303.

Corresponding Author

* Telephone: +972-4-8293562, E-mail: ozg@technion.ac.il

* Telephone: +1 413 545 6250, E-mail: fcjentoft@umass.edu

KEYWORDS C-C bond formation, cooperative catalysis, Henry reaction, functionalized silica, amine cooperativity, grafted amine catalysts

Abstract

The efficient promotion of cooperative catalytic interactions on solid surfaces can be of great benefit for a range of important reactions. Herein, we demonstrate that the cooperative interactions of isolated

tin (Sn) and titanium (Ti) sites on silica with grafted primary amines (NH_2) can be tuned by changing the immediate chemical environment of the metal sites (M). We show that by tethering various size organic ligands (RO) to the M sites, we can govern the interactions between the sites as measured by the presence of NH_3^+. We show that the concentration of NH_3^+ is directly correlated with the activity of the model Henry reaction. We further find that the selectivity to the olefinic product increased from 59% for the cooperative interactions of grafted NH_2 and surface silanols, to 84-92% for the cooperative interactions between grafted NH_2 and the isolated Sn or Ti sites. Analysis by DFT shows that these cooperative interactions are enabled by the presence of a trace amount (2 molecules per M site) of water near the metal sites and resulting hydrolysis, which depends on the hydrophobicity of the RO group and the nature of the metal. Hence, the current work provides advanced molecular-level insights on the underlying principles of cooperative interactions on a solid surface and guidance for governing such interactions by tuning the chemical environment.

1. Introduction

Cooperative heterogeneous catalysts are a class of materials that contain at least two active sites that work in concert to activate an electrophile and a nucleophile to promote a single chemical transformation.[1] The cooperative mechanism is accompanied by a lower activation energy, which allows conducting the reaction under milder conditions as well as increases the overall catalyst activity and may also lead to a higher selectivity, as compared with single-site catalyst analogs.[2] As such, this class of heterogeneous catalysts can make the overall chemical process significantly more environmentally-friendly. However, inducing and even more so controlling the cooperative catalytic interactions on a solid material is a challenging task.[1,3–5] To synthesize an efficient cooperative catalytic material, three architectural levels in material design need to be engineered: 1) the 3D structure of the support, 2) the immediate chemical environment surrounding the catalytic site and 3) the precise positioning and orientation of the catalytic sites.[3]

Materials involving amine sites grafted on amorphous silica have been extensively demonstrated to promote cooperative catalytic interactions for reactions such as the aldol condensation and others.[6–17] The liquid phase aldol condensation and nitroaldol condensation are an important class of reactions in green chemistry and enable the conversion of biomass-derived molecules to fuels and chemicals.[18] The Henry reaction (see **Figure 1**), specifically has been extensively used in literature as probe reaction to monitor changes in the level of cooperative interactions between grafted NH_2 and surface silanols.[15,16,19] Mechanistically, it was shown that the direct formation of the unsaturated product via the imine route is due to cooperative interactions between the NH_2 and surface silanol sites.[16] Therefore, the selectivity of the Henry reaction toward the unsaturated (olefinic) product serves as a descriptor for identifying cooperative interactions between the acid and base functions.

Studies of cooperative interactions between silanols on amorphous silica and grafted NH_2 allowed isolation of structural and chemical parameters affecting the cooperative interactions. Specifically, the effect of proximity and orientation between the OH and NH_2 on the surface,[20] acid-to-base ratio (OH:NH_2),[19] silica porosity,[19] and the immediate chemical environment surrounding the base site have all been rigorously evaluated.[16] However, because of its amorphous nature, silica is inherently nonuniform, leading to a nonrandom spatial distribution of grafted amines, which in turn leads to amine clustering and pore-blockage.[21] In addition, the rigid structure of silica restricts active site configurational movement, which has been shown to be important with respect to the efficiency of catalytic cooperativity.[20] The consequence of these limitation is evident in the separate works of both Moschetta et al. and Bass et al. In both works a maximum of ≈80% selectivity to the olefinic product of the Henry reaction of 4-nitrobenzaldehyde and nitromethane is reached using grafted propyl amines on silica as the catalyst.[13,16]

With the aim to improve the efficiency and control of cooperative interactions on solid surfaces, herein we examine the performance of isolated tin (Sn) and titanium (Ti) sites grafted separately on aminopropyl functionalized silica. These metals were specifically chosen as they have been shown to

function cooperatively with primary amine sites on the backbone of chitosan.[22,23] As previously reported for such metals, the hybrid coordination environment comprised of organic and inorganic ligands renders a material with improved hydrolytic and mechanical stability.[4] Specifically, grafted Ti and Sn sites on silica type materials have been demonstrated to be reactive and stable for a range of reactions.[24–27] By a combined experimental and computational analysis, we show that both the Sn and Ti sites catalyze the reaction cooperatively more efficiently than amine-functionalized SiO_2 but, only in the presence of a trace amount of water. We further show that the catalytic activity can be governed by manipulating the chemical environment, which is dictated by the size of a grafted alkoxy group.

2. Results and discussion

Briefly, the catalytic materials were prepared by grafting a metal (M) acid site of Sn or Ti on commercially available aminopropyl-functionalized silica (APS) using tetrachloride precursors, see ESI for full synthesis details. Notably, to avoid variations in the average amine surface concentration and distribution, the same batch was used for all grafted materials. The Sn or Ti sites were subsequently grafted with OH groups or different molecular size alkoxy groups through the exchange of the Cl ligand with an RO ligand. These obtained materials were denoted as RO-M/APS where M=Sn/Ti and R= H, CH_3, $CH(CH_3)_2$, $(CH_2)_2CH(CH_3)_2$, see **Figure 2**.

All materials were characterized using powder X-ray diffraction (PXRD), N_2-physisorption, diffuse reflectance UV-vis spectroscopy, diffusive reflectance infrared Fourier transform spectroscopy (DRIFTS) and X-ray photoelectron spectroscopy (XPS). The results for material characterization were cross referenced with kinetic measurements for the Henry reaction.

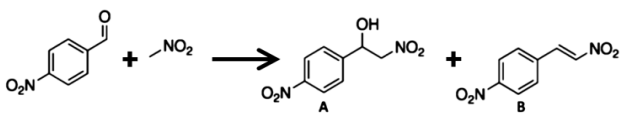

Figure 1. The Henry reaction of 4-nitrobenzaldehyde and nitromethane forms the alcoholic product (A) and unsaturated (olefinic) product (B)

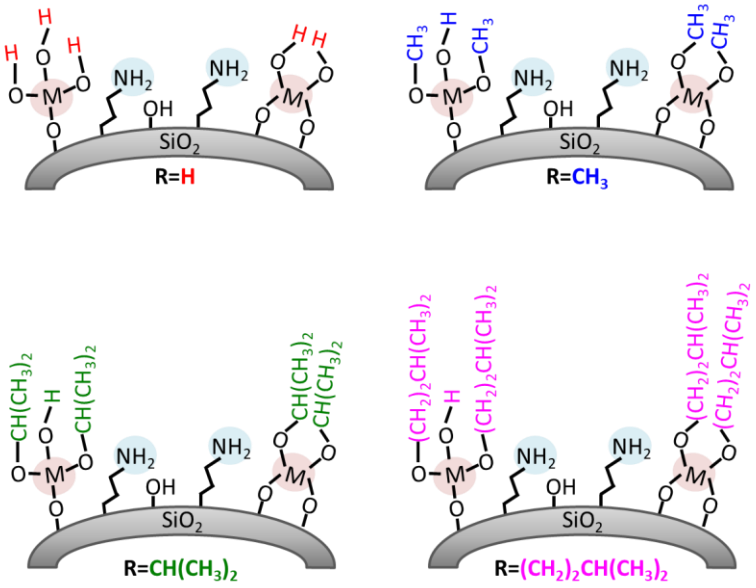

Figure 2. Schematic representation of the various RO-M/APS materials. The M represents Sn or Ti site. The grafting of the -OR groups was accomplished by initial grafting of either $SnCl_4$ or $TiCl_4$ to react with the Si-OH on the surface of APS, removal of excess precursor followed by the introduction of the -OR group, see SI file for detailed experimental information.

Materials characterization

Success of the metal grafting was evident from ICP-MS analysis, **Table 1**. The effect of the M grafting on the crystallinity of the APS is shown in the PXRD patterns of the RO-M/APS materials, **Figure 3**. All PXRD patterns show the presence of a wide peak at 2θ=22.2°, associated to amorphous silica.[28] Upon metal grafting, a new peak at 2θ=18.0° (d= 0.49 nm) was detected in both the RO-Sn/APS and RO-Ti/APS materials, which indicates the presence of a small amount of ordered material. The position of the new reflection does not match any of the reflections in the diffractograms of SnO_2 or TiO_2 phases.

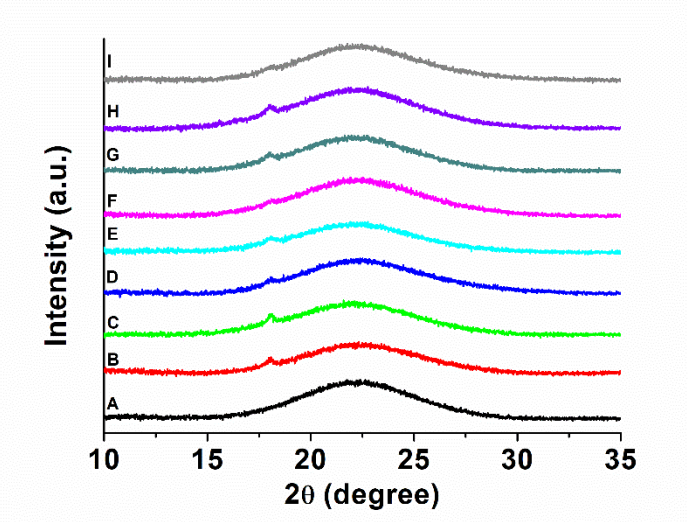

Figure 3. PXRD patterns for (**A**) native APS, (**B**) HO-Sn/APS, (**C**) CH_3O-Sn/APS, (**D**) $CH(CH_3)_2O$-Sn/APS, (**E**) $(CH_2)_2CH(CH_3)_2O$-Sn/APS, (**F**) HO-Ti/APS, (**G**) CH_3O-Ti/APS, (**H**) $CH(CH_3)_2O$-Ti/APS and (**I**) $(CH_2)_2CH(CH_3)_2O$-Ti/APS.

The effect of the M grafting on the APS surface area was determined from the N_2-physisorption analysis. The BET surface area values for all materials are summarized in **Table 1**, and the full N_2 adsorption-desorption curves are given in **Figure S1**. For all materials, the N_2-physisorption curves look very similar exhibiting an H2 (b) hysteresis loop (as defined by IUPAC), indicative of a complex pore structure with a dominant pore blocking factor.[29] The BET surface areas of the HO-M/APS and CH_3O-M/APS materials were in the range of 342-363 m^2g^{-1}. Whereas, the BET values of the $CH(CH_3)_2O$-M/APS and $(CH_2)_2CH(CH_3)_2O$-M/APS materials were in a slightly lower range of 295-335 m^2g^{-1}. The slight decrease in BET surface area is attributed to partial pore blocking due to the grafting of the larger RO groups.[30]

Table 1. BET surface area values for the RO-M/APS materials, from N_2-physisorption analysis.

	Sn/Ti content[a] ($mmol/g_{sample}$)	BET surface area (m^2g^{-1})
APS	0	352
HO-Sn/APS	0.13	355
CH_3O-Sn/APS	0.13	348
$CH(CH_3)_2O$-Sn/APS	0.13	317
$(CH_2)_2CH(CH_3)_2O$-Sn/APS	0.16	332
HO-Ti/APS	0.10	342
CH_3O-Ti/APS	0.17	363
$CH(CH_3)_2O$-Ti/APS	0.12	296
$(CH_2)_2CH(CH_3)_2O$-Ti/APS	0.11	335

[a] data obtained from ICP-OES

Because detection by X-ray powder diffraction requires a minimum crystalline domain size and concentration, the materials were also examined by diffuse reflectance UV-vis spectroscopy. The spectra in **Figure 4** demonstrate the absence of oxide particles. SnO_2 particles would be expected to show a band edge with a gap energy of 3.6 eV (345 nm)[31] and an onset at about 360 nm,[32,33] and TiO_2 (anatase) particles would be characterized by an edge position of 360 nm.[34] As seen in **Figure 4**, no such edge-type features were detectable at the anticipated wavelengths.

The spectra of the Sn-containing samples exhibit 1 or 2 bands in the range of 265 to 275 nm and an additional band at about 305 nm. Sn highly coordinated with oxido, hydroxido, and aqua ligands reportedly absorbs around 270 nm,[35] which matches well with the observed position. Wavelengths longer than 300 nm have been reported for octahedral tin with mixed ligands, for example keto or carboxylato ligands combined with chlorido ligands,[36,37] but also for $S_2O_7^{2-}$.[38] In the spectra of the Ti-containing samples, the intense short wavelength absorption at 214 nm can be assigned to LMCT (ligand-to-metal charge transfer) bands of isolated Ti^{4+} tetrahedrally coordinated with O^{2-}.[34,39] The broad shoulder towards longer wavelengths (~ 250 nm) is uncharacteristic and could imply the presence of titanium that is octahedrally coordinated with O^{2-} ligands, or tetrahedrally coordinated with mixed

ligands. Normalization of the spectra (**Figure S3**) shows that the variations in speciation among the titanium-containing samples are minor.

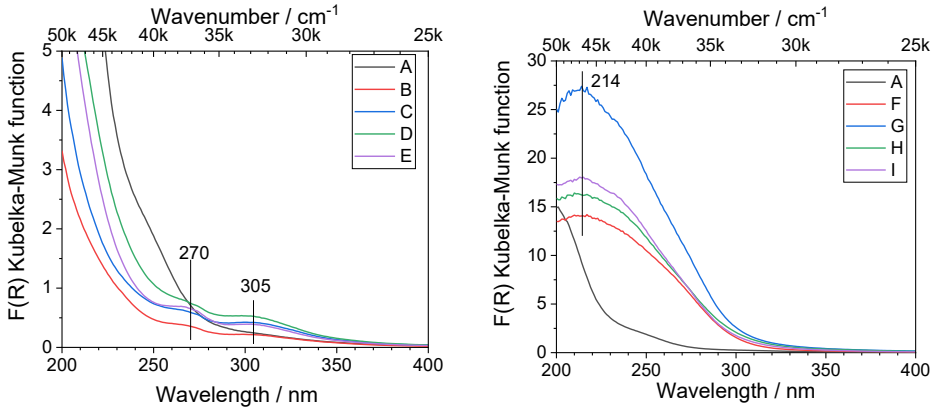

Figure 4: UV-vis spectra. (**A**) native APS, (**B**) HO-Sn/APS, (**C**) CH_3O-Sn/APS, (**D**) $CH(CH_3)_2O$-Sn/APS, (**E**) $(CH_2)_2CH(CH_3)_2O$-Sn/APS, (**F**) HO-Ti/APS, (**G**) CH_3O-Ti/APS, (**H**) $CH(CH_3)_2O$-Ti/APS and (**I**) $(CH_2)_2CH(CH_3)_2O$-Ti/APS.

DRIFTS was used to monitor the grafting process and the tethering of the RO groups, **Figure 5**. The APS showed vibrations characteristic of silica,[34] specifically, skeletal vibrations at 1220, 1085, 802, 560 and 465 cm^{-1}. Overtones of these vibrations were visible at 1986, 1873 and 1630 cm^{-1}. In addition, silanol groups stretching and deformation vibrations were observed at 3733 and 3650 cm^{-1}, and at ~ 950 cm^{-1}, respectively. Several CH-stretching bands between 2980 and 2865 cm^{-1} and CH deformation bands between 1476 and 1352 cm^{-1} arise from the aminopropyl groups, and possibly residual alkoxy groups from the grafting agent. The asymmetric stretching, symmetric stretching, and bending vibration of the NH_2 groups on APS are positioned at 3374, 3310 and 1598 cm^{-1}, respectively.[40] The band at 1625-1630 cm^{-1} may arise from bending modes of both the amine and water adsorbed on the surface. For example, White and Tripp associated vibrations at 1622 and 1596 cm^{-1} to free NH_2 groups and to NH_2 groups H-bonded to Si-OH, respectively.[41]

The observation of Sn-O-Si and Ti-O-Si vibrations can serve as direct evidence for metal grafting. In tetrahedral configuration, a band at 960 cm^{-1} is expected for Ti[34] and debated for Sn.[42] Unfortunately, the silanol deformation vibration at 950 cm^{-1} complicates the assessment of this region. In particular, materials treated with water (B and F in Figure 5, also see the overlay of spectra in Figure S4) show a more pronounced Si-OH stretching vibration at 3733 cm^{-1} in comparison with the APS spectrum, suggesting the corresponding deformation may contribute to an enhanced intensity around 960 cm^{-1}. The interpretation of the spectral region around 950-960 cm^{-1} is thus inconclusive. The better albeit indirect evidence for the grafting in the FTIR spectra is the change in the relative intensities in the region between ~1220 cm^{-1} and 1000 cm^{-1}. The region features two bands from the split asymmetric stretching mode of Si-O-Si bridges, possibly representing different ring sizes.[34] A change in the intensity ratio, together with the subtle variation in the shape of the corresponding Si-O-Si bending at 802 cm^{-1}, may imply preferential reaction of some SiO_2 surface sites during grafting. For the samples subjected to alcoholysis, the C–O stretching vibrations of the metal alkoxides are expected between ~1120 cm^{-1} and 990 cm^{-1}.[43–45] It is not possible to discern these contributions since the band shape for the M-OR samples in this region is between the shapes of APS and the samples subjected to hydrolysis.

The tethering of the different RO groups was confirmed by the appearance of stretching bands of CH_2 and CH_3 at ca. 3000-2800 cm^{-1}.[46] Some of the R-groups led to discernable new bands or increased intensity: 2853 cm^{-1} methoxy (from MeOH), 2980 $\nu_{as}CH_3$ (from IPA), and 2962 cm^{-1} $\nu_{as}CH_3$ and 2935 cm^{-1} $\nu_{as}CH_2$ (from isoamyl). Interestingly, the relative intensities of the bands at 3460, 3648 and 3730 cm^{-1}, which are related to surface hydroxy species,[47] were found to be characteristic of the specific RO group tethered to the M site. Specifically, water- or isopropyl alcohol-treated samples are characterized by more intense hydrogen bonding. The broad absorption bands from hydrogen bonding obscure the range of possible Ti-OH or Sn-OH vibrations.

Notably, following the grafting procedure a new band at ca. 1522 cm^{-1} was found, indicating the presence of NH_3^+ groups by their characteristic symmetric bending mode, while the NH_2 stretching

bands became less pronounced with respect to the bands of the Si-OH.[48] The intensity at around 1625 to 1630 cm^{-1} also increased and the position is consistent with the corresponding asymmetric bending mode of NH_3^+;[49] however, this band is of lower diagnostic value because of contributions of the silica skeletal vibration overtone and the deformation mode of possibly present adsorbed water.

The IR spectra demonstrate that acidic protons have been introduced through grafting of the metal compounds and subsequent hydrolysis or alcoholysis with trace hydrolysis, and that these protons have been transferred to amine groups to give alkylammonium cations.

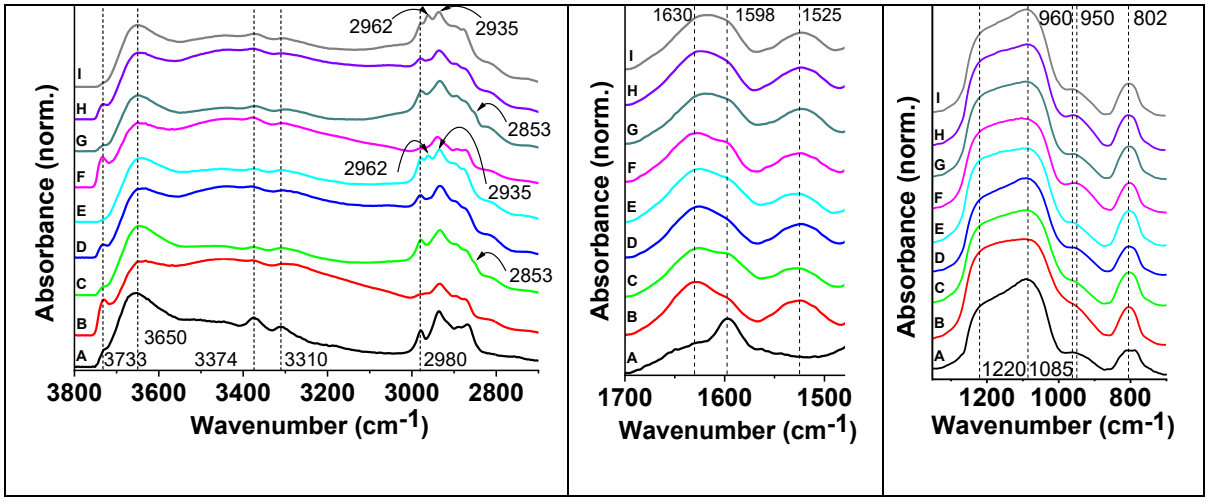

Figure 5. DRIFT spectra in the range of 3800-2600 cm^{-1}, 1700-1480 cm^{-1} and 1350-700 cm^{-1} for (**A**) native APS, (**B**) HO-Sn/APS, (**C**) CH_3O-Sn/APS, (**D**) $CH(CH_3)_2O$-Sn/APS, (**E**) $(CH_2)_2CH(CH_3)_2O$-Sn/APS, (**F**) HO-Ti/APS, (**G**) CH_3O-Ti/APS, (**H**) $CH(CH_3)_2O$-Ti/APS and (**I**) $(CH_2)_2CH(CH_3)_2O$-Ti/APS. Labels without arrows indicate positions of the vertical lines.

Analyzing the samples using XPS allowed quantification of the extent of interaction between the M-OH and adjacent NH_2 sites. The core level spectra for all the RO-Sn/APS and RO-Ti/APS materials were recorded for C1s, O1s, N1s, **Figure 6** and for Sn3d and Ti2p, **Figure S2**. The O1s spectra of all

the RO-Sn/APS materials showed the formation of a peak at 531.9 ± 0.2 eV attributed to Sn-O-C and Sn-OH bonds following grafting, **Figure 6**.[50,51] In all samples the O1s peak at 531± 0.1 eV corresponds to the Si-O of the grafted aminopropyl silane.[52] The O1s spectra of the RO-Ti/APS materials showed the formation of two peaks at 530.0 ± 0.1 eV and 531.9 ± 0.1 eV corresponding to Ti-O-C and Ti-OH bonds, respectively.[53] The grafting of the M sites to the silica surface was accompanied by a decrease in the peak area at 533.6 ± 0.2 eV attributed to the Si-OH bond,[54] showing that the grafting occurred through the silica surface hydroxy groups. This gives us the ability to calculate for each sample the ratio between the amount of M-O-R bonds formed and the number of Si-OH groups reacted, **Table 2**. It can be seen that for all samples the $M\text{-}O\text{-}R_{formed}/Si\text{-}OH_{reacted}$ ratio was greater than 1, which indicates that the number of -OR groups is equal or greater than the number of M-O-Si bonds. For tetrahedral configuration, the ratio suggests that the M sites are grafted in a monodentate ($Si\text{-}O\text{-}M\text{-}(O\text{-}R)_3$) or bidentate ($(Si\text{-}O)_2\text{-}M\text{-}(O\text{-}R)_2$) configuration, which is typical for room temperature grafting.[55] Interestingly, the $M\text{-}O\text{-}R_{formed}/Si\text{-}OH_{reacted}$ ratio was found to be specific for the type of RO group tethered to the M site. Hence, it can be assumed that each of the R-OH molecules has a specific affinity to the Cl-M site.

From the O1s XP spectra of the RO-Ti/APS materials it was found that the Ti-OH/Ti-O-C ratios for the CH_3O-Ti/APS, $CH(CH_3)_2O$-Ti/APS and $(CH_2)_2CH(CH_3)_2O$-Ti/APS materials were 2.2 ± 0.4, 1.5 ± 0.3 and 3.3 ± 0.7, respectively. This clearly shows that each Ti site is coordinated to at least one OR ligand. The remaining M-Cl sites formed Ti-OH, most likely due to reaction with trace water in the grafting solution. The same analysis could not be done for the Sn system as the O1s peaks of the Sn-O and Sn-OR overlap completely.

The N1s signal of the native APS material shows a peak at 399.15 ± 0.2 eV corresponding to the existence of NH_2 species only, which was typically reported to appear at 399.3-399.5 eV.[56,57] Upon M grafting, a new peak appears at 401.4-401.6 ± 0.2 eV, which is attributed to the formation of protonated

NH_3^+, **Figure 6**.[56,58] The formation of NH_3^+ species following M grafting is consistent with the DRIFTS results above and accounts for 20 to 45% of the total amine present in the samples. Notably, in the presence of the excess triethylamine the metal chlorides may also react to form a Sn/Ti-amide bond.[57] Farfan-Arribas et al. reported the appearance of a 401.1 eV band related to a Ti-amide bond following the adsorption of dimethyl amine on TiO_2.[59] Head et al. attributed binding energies of 398.6 eV and 400.3 eV to the presence of Ti-amide in neutral and protonated form, respectively.[60] These observations and our own show that the N1s peak is significantly dependent on the chemical environment. Although we cannot rule out the formation of a metal-amide bond, based on the DRIFT data discussed above, we relate the higher binding energy XP peak here to amine protonation by the interaction of the amine with an adjacent species. Moreover, the grafting procedure is conducted in the presence of triethylamine, which scavenges free HCl in solution, thus preventing formation of NH_3^+ species through amine protonation by HCl.[23]

Based on the XPS atomic concentration precent (AC%) we find that in all the grafted samples the atomic % of N in the NH_3^+ form is greater than the atomic % of residual Cl, **Table 3**, which originates from a partially substituted M site. Assuming that each residual Cl atom accounts for the formation of one NH_3^+ the % excess of NH_3^+ species, exceeding the amount of residual Cl, can be calculated to be 9-33% for the Sn system and 4-34% for the Ti system, **Table 3**.

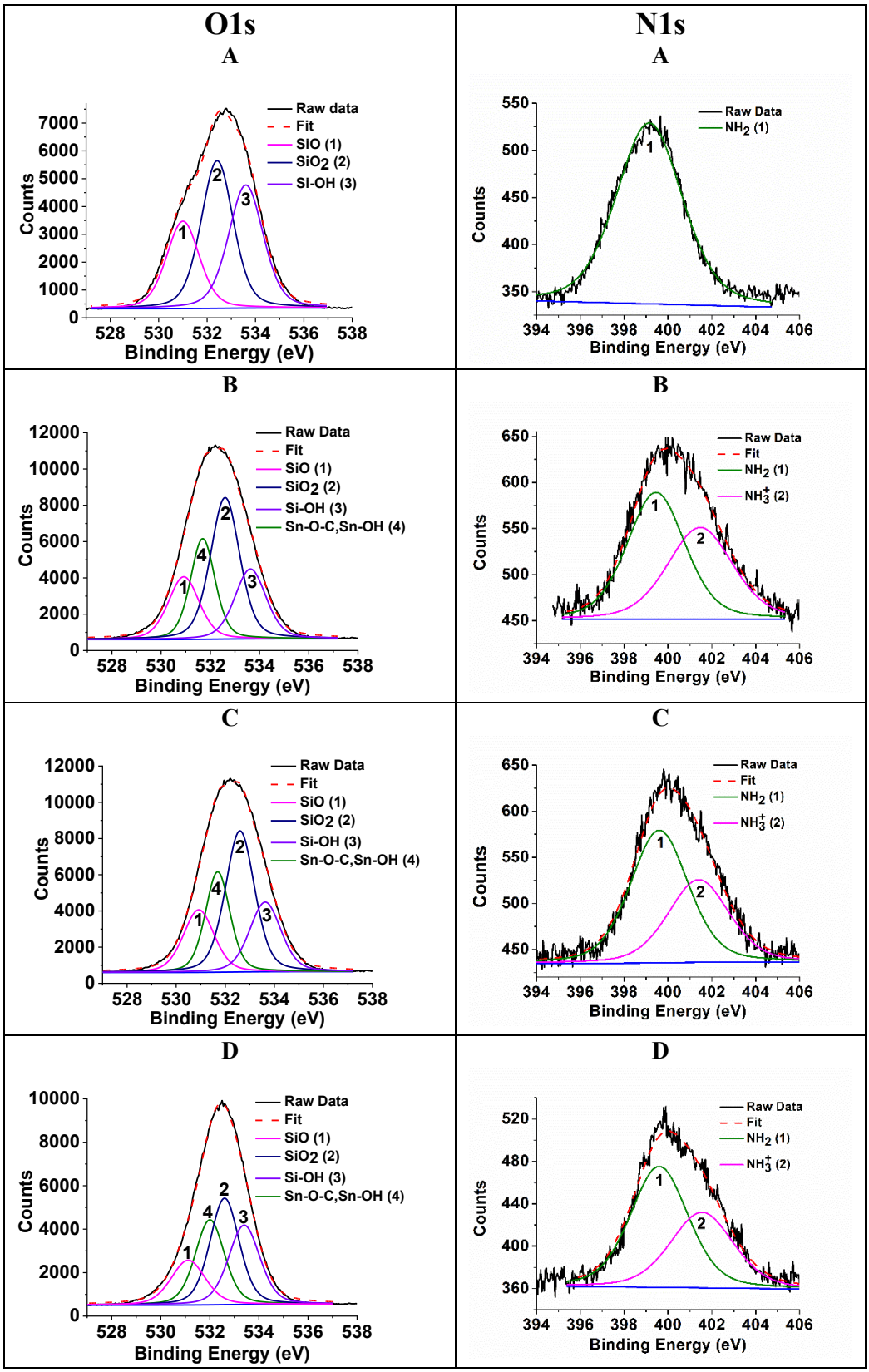
O1s
A
Raw data
Fit
SiO (1)
SiO2 (2)
Si-OH (3)
Counts
Binding Energy (eV)
N1s
A
Raw Data
NH2 (1)
Counts
Binding Energy (eV)
B
Raw Data
Fit
SiO (1)
SiO2 (2)
Si-OH (3)
Sn-O-C,Sn-OH (4)
Counts
Binding Energy (eV)
B
Raw Data
Fit
NH2 (1)
NH3+ (2)
Counts
Binding Energy (eV)
C
Raw Data
Fit
SiO (1)
SiO2 (2)
Si-OH (3)
Sn-O-C,Sn-OH (4)
Counts
Binding Energy (eV)
C
Raw Data
Fit
NH2 (1)
NH3+ (2)
Counts
Binding Energy (eV)
D
Raw Data
Fit
SiO (1)
SiO2 (2)
Si-OH (3)
Sn-O-C,Sn-OH (4)
Counts
Binding Energy (eV)
D
Raw Data
Fit
NH2 (1)
NH3+ (2)
Counts
Binding Energy (eV)

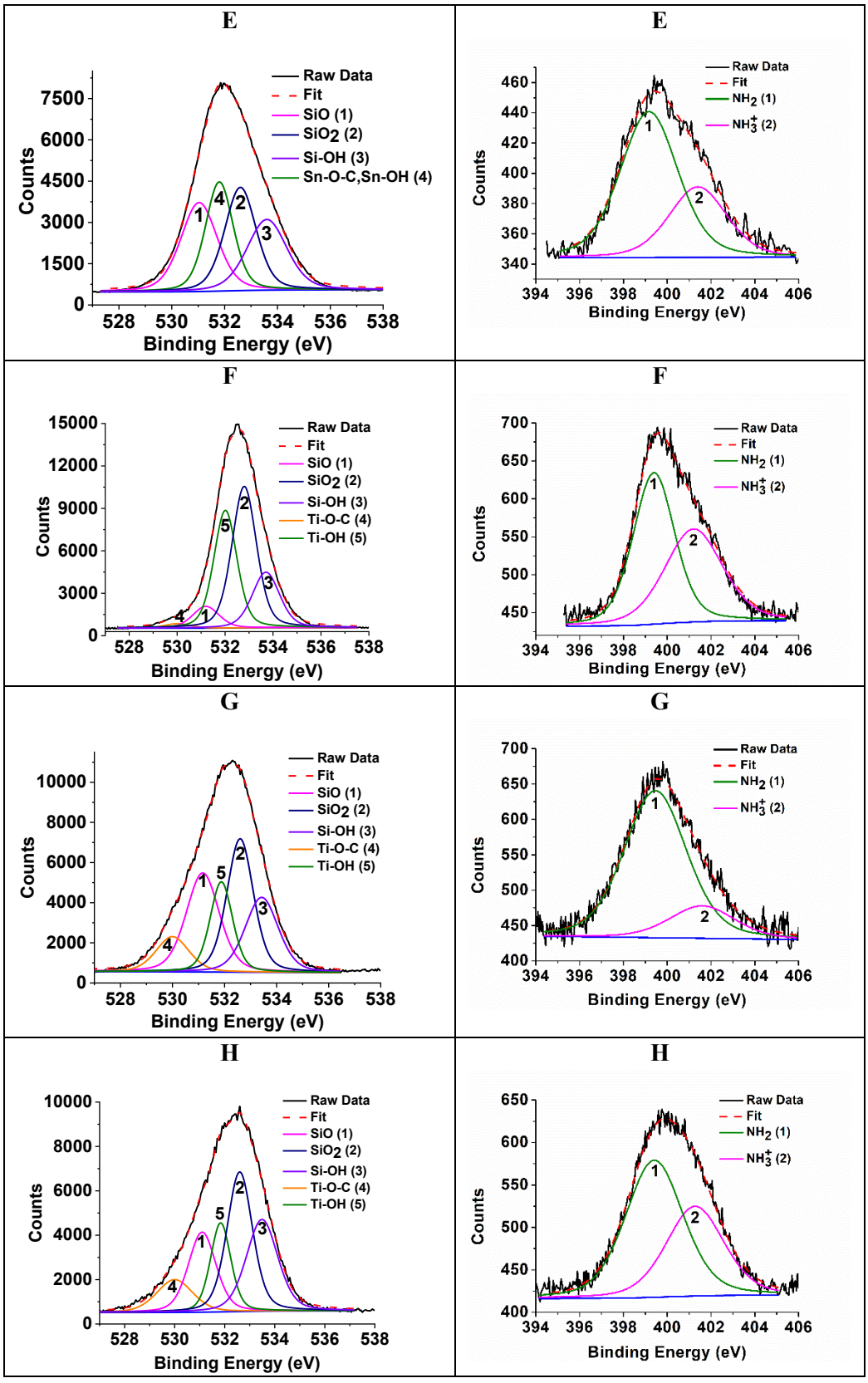
E
Raw Data
Fit
SiO (1)
SiO2 (2)
Si-OH (3)
Sn-O-C,Sn-OH (4)
Counts
Binding Energy (eV)
E
Raw Data
Fit
NH2 (1)
NH3+ (2)
Counts
Binding Energy (eV)
F
Raw Data
Fit
SiO (1)
SiO2 (2)
Si-OH (3)
Ti-O-C (4)
Ti-OH (5)
Counts
Binding Energy (eV)
F
Raw Data
Fit
NH2 (1)
NH3+ (2)
Counts
Binding Energy (eV)
G
Raw Data
Fit
SiO (1)
SiO2 (2)
Si-OH (3)
Ti-O-C (4)
Ti-OH (5)
Counts
Binding Energy (eV)
G
Raw Data
Fit
NH2 (1)
NH3+ (2)
Counts
Binding Energy (eV)
H
Raw Data
Fit
SiO (1)
SiO2 (2)
Si-OH (3)
Ti-O-C (4)
Ti-OH (5)
Counts
Binding Energy (eV)
H
Raw Data
Fit
NH2 (1)
NH3+ (2)
Counts
Binding Energy (eV)

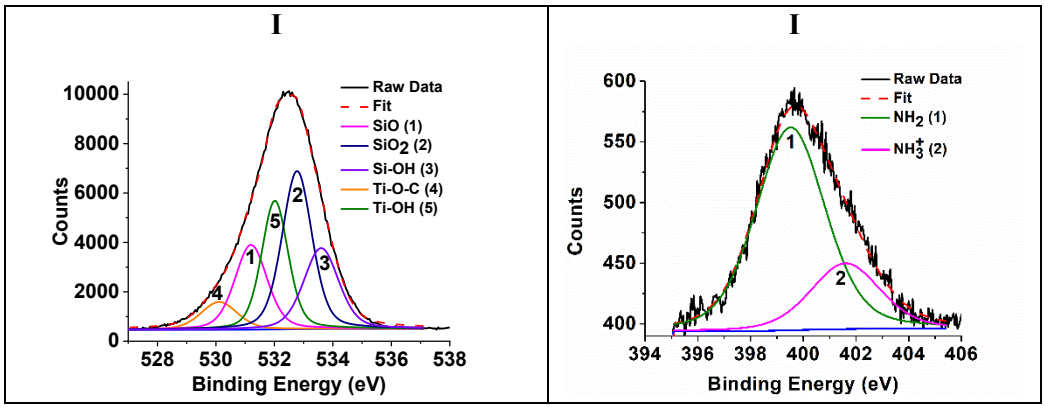

Figure 6. XPS spectra of O1s and N1s core levels for (**A**) native APS, (**B**) HO-Sn/APS, (**C**) CH_3O-Sn/APS, (**D**) $CH(CH_3)_2O$-Sn/APS, (**E**) $(CH_2)_2CH(CH_3)_2O$-Sn/APS, (**F**) HO-Ti/APS, (**G**) CH_3O-Ti/APS, (**H**) $CH(CH_3)_2O$-Ti/APS and (**I**) $(CH_2)_2CH(CH_3)_2O$-Ti/APS.

Table 2. Calculated surface atomic concentrations (%AC) of O, M-O-R_{formed}/Si-$OH_{reacted}$ ratios on the RO-M/APS catalyst surface, and Ti-O-C/Ti-OH ratios on the RO-Ti/APS catalyst surface, from XPS analysis.

	O AC%	M-O-R_{formed}/Si-$OH_{reacted}$*	Ti-OH /Ti-O-C
APS	55±1	-	
HO-Sn/APS	57±1	1.4±0.3	
CH_3O-Sn/APS	55±1	1.3±0.3	
$CH(CH_3)_2O$-Sn/APS	55±1	2.3±0.5	
$(CH_2)_2CH(CH_3)_2O$-Sn/APS	55±1	2.0±0.4	
HO-Ti/APS	57±2	2.0±0.4	
CH_3O-Ti/APS	56±1	3.3±0.7	2.2±0.4
$CH(CH_3)_2O$-Ti/APS	54±1	2.3±0.5	1.5±0.3
$(CH_2)_2CH(CH_3)_2O$-Ti/APS	54±1	1.6±0.3	3.3±0.7

*The M-O-R_{formed}/Si-$OH_{reacted}$ and Ti-OH/Ti-O-C ratios were calculated from the area % of the M-O-R, Si-OH, Ti-OH and Ti-O-C peaks obtained from the deconvolution of the high resolution O1s XPS spectra. The error in AC based on XPS instrument parameters is 20%.

Table 3. Calculated surface atomic concentrations (%AC) of N, Cl, N in NH_3^+ form and excess % of NH_3^+ on the RO-M/APS catalyst surface, from XPS analysis.

	N AC%	Cl AC%	AC% of N in NH_3^+ form	Excess % of NH_3^+ **	AC% of Ti-OH
APS	3.0±0.5	-	-	-	
HO-Sn/APS	2.7±0.5	0.30±0.06	1.2±0.2	33±9	
CH_3O-Sn/APS	2.5±0.5	0.42±0.08	1.0±0.2	23±6	
$CH(CH_3)_2O$-Sn/APS	2.3±0.5	0.6±0.1	0.9±0.2	13±3	
$(CH_2)_2CH(CH_3)_2O$-Sn/APS	2.3±0.5	0.5±0.1	0.7±0.1	9±2	
HO-Ti/APS	2.7±0.5	0.28±0.06	1.2±0.2	34±9	0.8±0.2
CH_3O-Ti/APS	2.7±0.5	0.5±0.1	1.2±0.2	25±7	0.8±0.2
$CH(CH_3)_2O$-Ti/APS	2.7±0.5	0.7±0.1	1.1±0.2	15±4	0.9±0.2
$(CH_2)_2CH(CH_3)_2O$-Ti/APS	2.4±0.5	0.5±0.1	0.6±0.1	4±1	0.8±0.2

**The AC% of NH_3^+ for each sample was calculated from the area % of the NH_2 and NH_3^+ peaks obtained from the deconvolution of the high resolution N1s XPS spectra. The error in AC% based on XPS instrument parameters is ±20%.

We use density functional theory (DFT) calculations to rationalize the excess NH^{3+} species (more details can be found in the **SI**) discussed above. Specifically, our calculations show that the isolated OH group on the metal (e.g., (OSi)X-Sn-OH) is unlikely to transfer a proton to the amine group. For example, the formation of the $^-$O-Sn-$(OCH_3)_2$ state was unstable, and the structure reverted back to an uncharged state. However, when two water molecules were added to the metal to form a stable octahedral complex, the proton readily transferred from a water molecule to the amine group, forming an ammonium cation and leaving an OH- ligand on the metal, which correlates well with previous work studying amines on silica surfaces. For example, Mafra et. al. demonstrated that the presence of a water molecule is required to stabilize a charged carbamic acid-like species.[61] **Figure 7a** and **Figure 7b** show that the charge-separated state is stabilized by strong electrostatic interaction between the proton and the Sn complex.

The electronic energies of the intermediates show that forming a charged complex is energetically favorable for both Sn and Ti. As can be seen in **Figure 7c**, Sn more readily adsorbs water and participates in charge transfer compared to Ti.

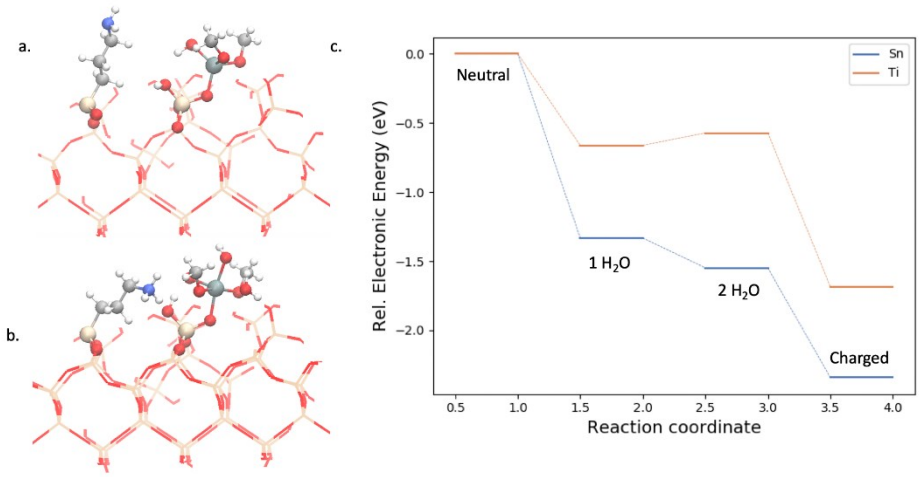

Figure 7. DFT analysis of materials, (a) shows the initial state with a 4-coordinate Sn complex. (b) shows the hexacoordinate Sn complex with an OH^- ligand and charged amine in close proximity. (c) shows the relative electronic energies moving from 4-coordinate metal to the final charged complex.

Since the presence of a protic solvent is necessary to facilitate charge transfer between the metal and the amine, this suggests that longer hydrocarbon chains on the metal would exclude protic solvent and result in a more nonpolar environment near the surface. Both of these factors would reduce the population of a charged complex near the surface, which matches the experimental results showing fewer charged complexes in catalysts with longer sidechains, **Figure 8**. Although the current analysis is limited to the 'static' structures, incorporating the flexibility of the organic groups is computationally intensive and is beyond the scope of this study.

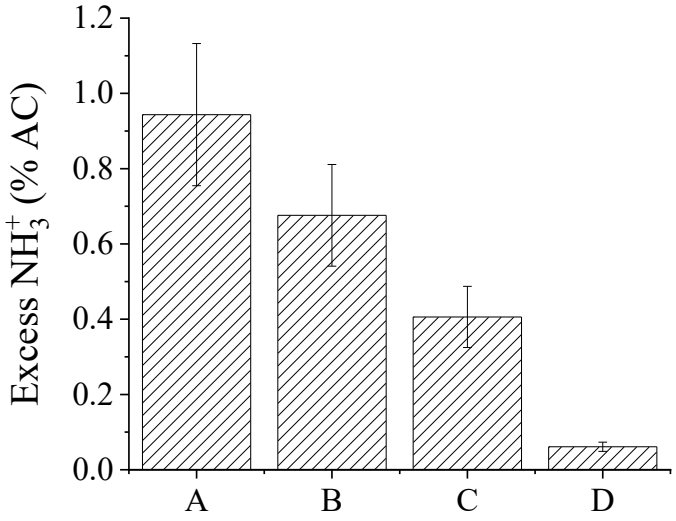

Figure 8. Excess AC% of NH_3^+ as a function RO group tethered to the Ti site for: HO-Ti/APS (A); CH_3O-Ti/APS (B); $CH(CH_3)_2O$-Ti/APS (C); $(CH_2)_2CH(CH_3)_2O$-Ti/APS (D)

Catalytic testing

The RO-M/APS materials described above were tested as catalysts for the Henry reaction of 4-nitrobenzaldehyde and nitromethane at 80 °C. The effect of surface NH_2 loading in each catalyst was normalized by adjusting the amount of catalyst in the reaction to have a total of $6.25x10^{-3}$ mmol, maintaining a constant 1/100 ratio of NH_2 sites to the 4-nitrobenzaldehyde. The amount of accessible amine sites was quantified using salicylaldehyde back titration, see details in the ESI and Table S1.

The reaction progress was followed by ^1H NMR using nitrobenzene as an internal standard. The initial rates for 4-nitrobenzaldehyde conversion and selectivity to the olefinic product were found to be higher for all the grafted materials as compared to APS control, **Figure 9**. The conversion obtained using the HO-Sn/APS and HO-Ti/APS catalysts was ~2-fold higher, after 60 min reaction, as compared to the APS. According to the computational analysis shown above, Sn more readily adsorbs water and participates in charge transfer, which can perhaps explain the higher catalytic performance of the Sn-based catalyst. It can

also be seen that the reaction conversion was correlated to the type of grafted RO maintaining the same trend (HO >CH_3O > $CH(CH_3)_2O$ > $(CH_2)_2CH(CH_3)_2O$) for both the Sn and Ti materials. This result is consistent with the results presented in **Figure 8**, which showed a dependence between the chain length of the RO ligand and the excess NH_3^+ species.

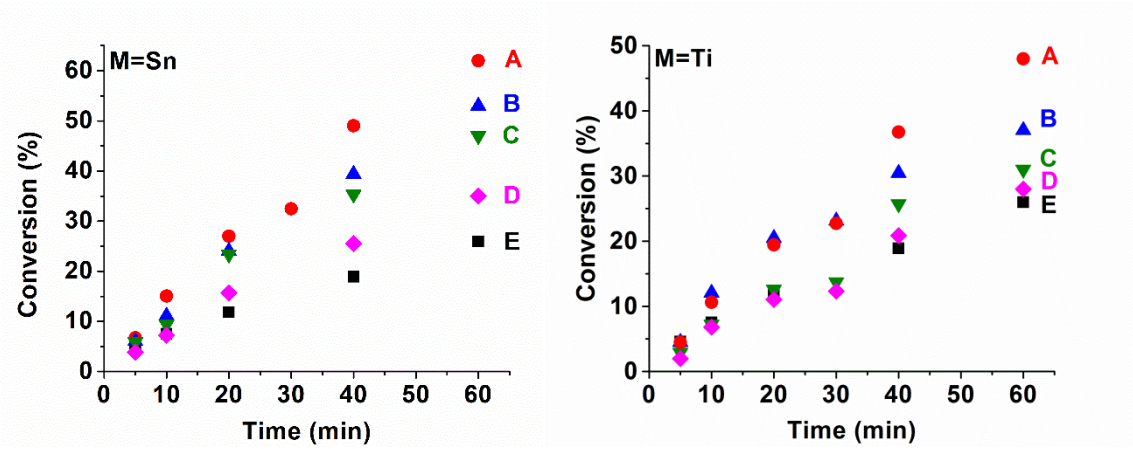

Figure 9. Conversion of 4-nitrobenzaldehyde vs. time for (**A**) HO-M/APS, (**B**) CH_3O-M/APS, (**C**) $CH(CH_3)_2O$-M/APS, (**D**) $(CH_2)_2CH(CH_3)_2O$-M/APS and (**E**) native APS. The reaction was run in a batch mode at 80 ºC with a ratio of 1/100 between the NH_2 sites and the constraining reactant 4-nitrobenzaldehyde.

Interestingly, a plot of the initial rates obtained for the various catalysts (Figure S5) as a function of the amount of excess NH_3^+ gives a linear trend for both the Sn and Ti materials, **Figure 10**. These results further show that the concentration of excess NH_3^+ groups is a descriptor for enhanced catalytic performance. It can also be observed that the obtained initial rates of the RO-Sn/APS materials were ~2-fold faster than those of the RO-Ti/APS materials, which is consistent with a more efficient cooperative interactions between the NH_2 and Sn-OH as compared to the interactions of the NH_2 and Ti-OH.

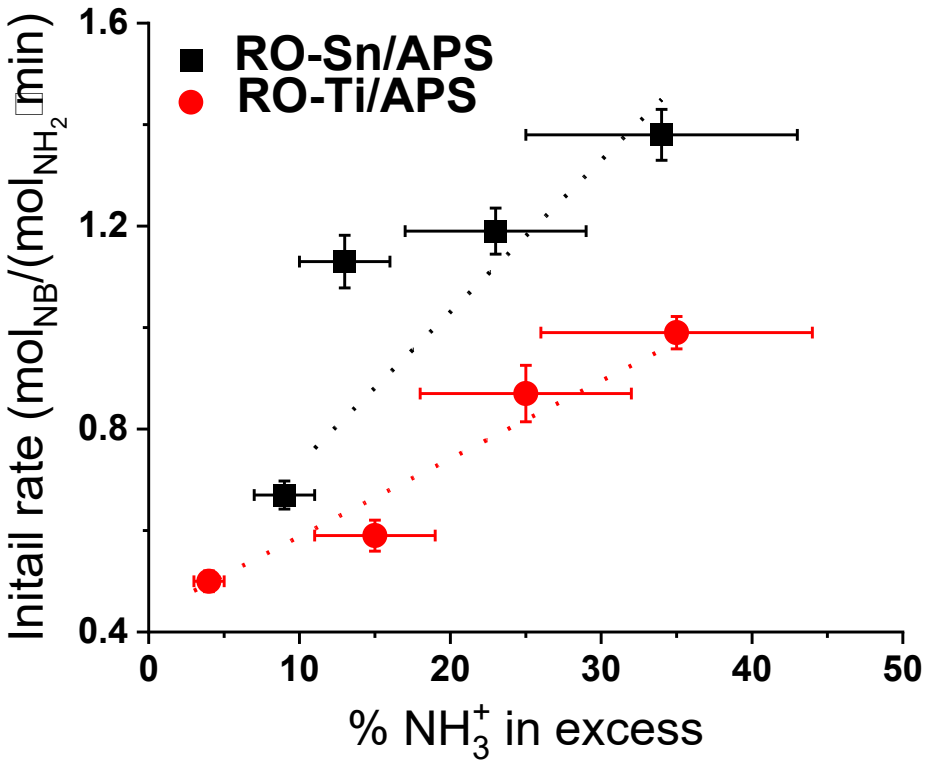

Figure 10. Initial rate for the Henry reaction obtained for the RO-M/APS catalysts vs. NH_3^+ species in excess estimated from XPS measurement, which represents the degree of coordination between the NH_2 and M-OH sites.

Plotting the initial rate (**Figure S4**) versus the ratio of excess NH_3^+ to M-OH sites is shown to give a linear trend, which correlates well with the bulkiness of the grafted molecule, **Figure 11**. This trend highlights the effect of the immediate chemical environment of the M site, as dictated by the size of the grafted RO. Where the bulkier hydrocarbon chain excludes water more efficiently from the surface and results in a more nonpolar environment near the M site, reducing the ability of the M-OH sites to interact the NH_2 sites and facilitate the proton transfer and formation of the excess NH_3^+.

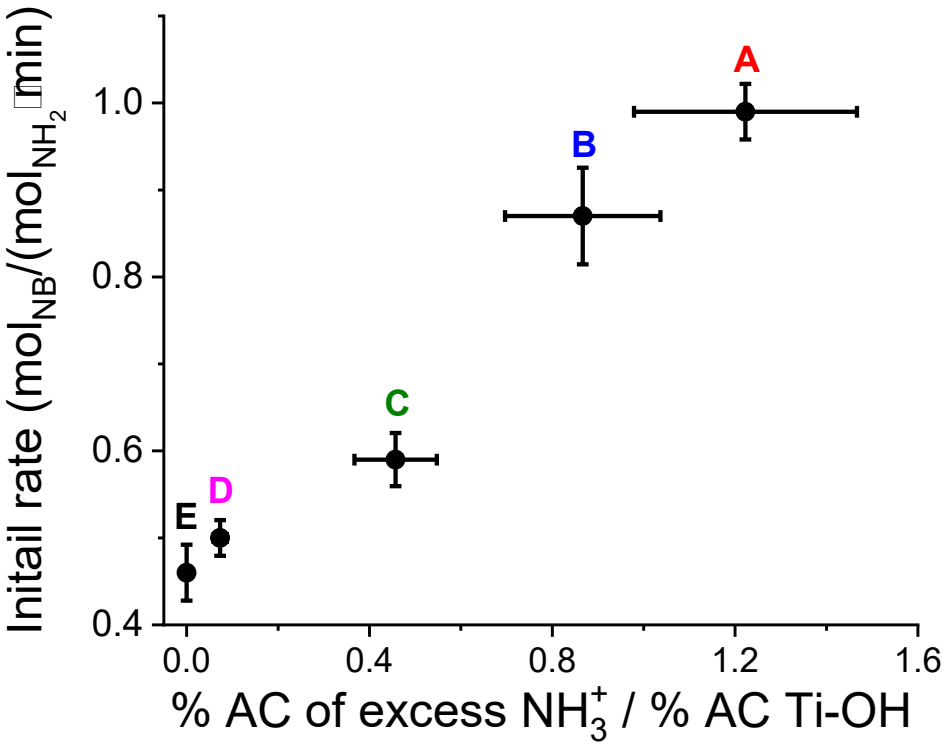

Figure 11. Initial rate for the Henry reaction obtained for the RO-Ti/APS catalysts vs. the calculated ratio between the AC% excess of NH_3^+ to AC% of Ti-OH bonds. (**A**) HO-M/APS, (**B**) CH_3O-M/APS, (**C**) $CH(CH_3)_2O$-M/APS, (**D**) $(CH_2)_2CH(CH_3)_2O$-M/APS and (**E**) native APS.

The selectivity data in **Table 4** show that the reaction catalyzed by APS was only 59% selective to the olefinic product, whereas Bass et al.[16], who used a similar NH_2-SiO_2 catalyst, obtained ~80% selectivity to the olefinic product. This difference is attributed to lower amine loadings, 0.7 mmolg^{-1} in this work as opposed to 1.3 mmolg^{-1} in the work of Bass et al. as well as to the higher reaction temperature, 80 ^{o}C in this work vs. 40 ^{o}C in the work of Bass et al. The change in the surface concentration and temperature is directly connected to the ability of the amine to interact with the surface hydroxy groups on silica and in-turn the reaction selectivity.[19,22] Interestingly, the reaction catalyzed by the RO-M/APS catalysts gave 84-92%, which suggests that cooperative interaction between NH_2 and Sn/Ti-OH sites are more efficient as compared to the NH_2-silanols interactions.

Table 4. Selectivity to the olefinic product averaged following 10, 20, 40 and 60 min of reaction.

Catalyst	Selectivity (%)
APS	59±2
HO-Sn/APS	84±1
CH_3O-Sn/APS	90±1
$CH(CH_3)_2O$-Sn/APS	91±3
$(CH_2)_2CH(CH_3)_2O$-Sn/APS	92±1
HO-Ti/APS	87.9±0.8
CH_3O-Ti/APS	87±2
$CH(CH_3)_2O$-Ti/APS	91±2
$(CH_2)_2CH(CH_3)_2O$-Ti/APS	90±1

To validate that indeed the NH_2 and the M-OH sites catalyze the Henry reaction in a cooperative manner rather than in a bi-functional manner, we tested the catalytic activity in the absence of a surface amine. The catalyst used were unmodified fumed silica (FS), and $(CH_2)_2CH(CH_3)_2O$-M-grafted on fumed silica, designated as $(CH_2)_2CH(CH_3)_2$-M/FS. The reaction was performed by adding either the FS or the $(CH_2)_2CH(CH_3)_2O$-M/FS catalysts to a mixture containing the reactants and both the alcoholic and olefinic products. The results showed that the FS was not active for the Henry reaction. However, both the $(CH_2)_2CH(CH_3)_2O$-Sn/FS and $(CH_2)_2CH(CH_3)_2O$-Ti/FS materials catalyzed the formation of the alcoholic product with 4 and 14% additional conversion, respectively. In both cases the initial amount of the olefinic product was not changed. We note that the XPS survey data (**Figure S6c**) of the Sn-modified FS shows the presence of a small peak corresponding to N1s. Whereas, both the Ti-modified FS and the FS, that was treated similarly (without adding the MCl_4), do not show the presence of N species (**Figure S6 a and b**). This suggests that either there is residual trace amount of triethylamine left or that the grafted M-OH sites on silica are slightly more acidic than the Si-OH, allowing them to catalyze the aldol reaction but, not the following dehydration reaction. Hence, we conclude that in the presence of the grafted primary amines (i.e. the RO-M/APS catalysts), the M-OH sites are able to promote cooperative interactions, which produce directly the olefinic product. This

result is consistent with previous results from our group using grafted metal sites on the backbone of chitosan.[22]

3. Conclusions

In this work, the surface of amino propyl-functionalized silica (APS) was grafted with Ti or Sn as isolated sites followed by tethering of various sizes of RO- groups. Catalytic testing for the Henry reaction showed that the Sn or Ti grafting resulted in a higher activity and significantly higher selectivity of 84% to 92% to the olefinic product, as compared to the APS control, which showed only 59%. It is shown that the grafting of Ti and Sn formed a new active site, composed of the cooperative interaction of the M-OH and an adjacent amine. Computational analysis showed that the cooperative interactions and the formation of the stable excess NH_3^+ species became possible only by the presence of a trace amount of polar solvent (e.g. 2 water molecules per M site). The amount of excess NH_3^+ was shown to be dependent on the size of the alkyl chain. Moreover, it was shown that the shortest RO-M groups (OH-M) were the most active and two-fold more active than Si-OH. In conclusion, this work shows that the introduction of a surface heteroatom (Ti or Sn) on silica provides a new avenue for significantly improving the cooperative interactions between grafted amines and surface metal hydroxy over the performance of the well-studied APS system. Moreover, it is shown that the catalytic performance can be controlled by tailoring the close chemical environment of the active site.

4. Acknowledgments

Author C. Khoury gratefully acknowledges the Neubauer Family Foundation for the support through the excellence scholarship. The work was supported by the Israeli Science Foundation (grant number 1266/17) and the Binational Science Foundation-National Science Foundation (grant number 2017639) and the Grand Technion Energy Program. This material is based upon work supported by the National Science Foundation under Grant No. 1804041. Dr. Guy Ankonina from the Technion and Professor Elad Gross from the Hebrew University are greatly appreciated for their help with diffuse reflectance UV-

vis measurements. Author FCJ acknowledges support through a Lady Davis Visiting Professorship.

Supporting information

The following file is available free of charge on the ACS Publications website at DOI:????. The file includes: Detailed experimental procedures, Figures S1-S6 and Table S1. Related to ^{1}H NMR, N_2 adsorption-desorption, additional XPS measurements, UV-vis, accessible amines quantification and initial rate plots.

5. References

(1) Margelefsky, E. L.; Zeidan, R. K.; Davis, M. E. Cooperative Catalysis by Silica-Supported Organic Functional Groups. *Chemical Society Reviews* **2008**, *37* (6), 1118–1126. https://doi.org/10.1039/B710334B.

(2) Aguila, B.; Sun, Q.; Wang, X.; O'Rourke, E.; Al-Enizi, A. M.; Nafady, A.; Ma, S. Lower Activation Energy for Catalytic Reactions through Host–Guest Cooperation within Metal–Organic Frameworks. *Angewandte Chemie - International Edition* **2018**, *57* (32), 10107–10111. https://doi.org/10.1002/anie.201803081.

(3) Khoury, C.; Gadipelly, C.; Pappuru, S.; Shpasser, D.; Gazit, O. M. Progress in the Design of Cooperative Heterogeneous Catalytic Materials for C-C Bond Formation. *Advanced Functional Materials* **2019**, *30* (18), 1901385. https://doi.org/10.1002/adfm.201901385.

(4) Diaz, U.; Brunel, D.; Corma, A. Catalysis Using Multifunctional Organosiliceous Hybrid Materials. *Chemical Society Reviews* **2013**, *42* (9), 4083. https://doi.org/10.1039/C2CS35385G.

(5) Fernandes, A. E.; Jonas, A. M. Design and Engineering of Multifunctional Silica-Supported Cooperative Catalysts. *Catalysis Today* **2018**. https://doi.org/10.1016/j.cattod.2018.11.040.

(6) Shylesh, S.; Hanna, D.; Gomes, J.; Krishna, S.; Canlas, C. G.; Head-Gordon, M.; Bell, A. T. Tailoring the Cooperative Acid-Base Effects in Silica-Supported Amine Catalysts: Applications in the Continuous Gas-Phase Self-Condensation of n-Butanal. *ChemCatChem* **2014**, *6* (5), 1283–1290. https://doi.org/10.1002/cctc.201301087.

(7) Brunelli, N. A.; Venkatasubbaiah, K.; Jones, C. W. Cooperative Catalysis with Acid-Base Bifunctional Mesoporous Silica: Impact of Grafting and Co-Condensation

Synthesis Methods on Material Structure and Catalytic Properties. *Chemistry of Materials* **2012**, *24* (13), 2433–2442. https://doi.org/10.1021/cm300753z.

(8) Brunelli, N. A.; Didas, S. A.; Venkatasubbaiah, K.; Jones, C. W. Tuning Cooperativity by Controlling the Linker Length of Silica-Supported Amines in Catalysis and CO 2 Capture. *J Am Chem Soc* **2012**, *134* (34), 13950–13953. https://doi.org/10.1021/ja305601g.

(9) Xie, J.; Ellebracht, N. C.; Jones, C. W. Inter- and Intramolecular Cooperativity Effects in Alkanolamine-Based Acid-Base Heterogeneous Organocatalysts. *ACS Omega* **2019**, *4* (1), 1110–1117. https://doi.org/10.1021/acsomega.8b02690.

(10) He, J.; An, Z.; He, J.; Dai, Y.; Yu, C.; Li, B. Enhanced Heterogeneous Asymmetric Catalysis via the Acid-Base Cooperation between Achiral Silanols of Mesoporous Supports and Immobilized Chiral Amines. *Journal of Catalysis* **2014**, *317*, 105–113. https://doi.org/10.1016/j.jcat.2014.06.012.

(11) Motokura, K.; Tada, M.; Iwasawa, Y. Cooperative Catalysis of Primary and Tertiary Amines Immobilized on Oxide Surfaces for One-Pot C-C Bond Forming Reactions. *Angewandte Chemie - International Edition* **2008**, *47* (48), 9230–9235. https://doi.org/10.1002/anie.200802515.

(12) Motokura, K.; Viswanadham, N.; Dhar, G. M.; Iwasawa, Y. Creation of Acid-Base Bifunctional Catalysis for Efficient C{single Bond}C Coupling Reactions by Amines Immobilization on SiO2, Silica-Alumina, and Nano-H-ZSM-5. *Catalysis Today* **2009**, *141* (1–2), 19–24. https://doi.org/10.1016/j.cattod.2008.04.011.

(13) Moschetta, E. G.; Brunelli, N. A.; Jones, C. W. Reaction-Dependent Heteroatom Modification of Acid-Base Catalytic Cooperativity in Aminosilica Materials. *Applied Catalysis A: General* **2015**, *504*, 429–439. https://doi.org/10.1016/j.apcata.2014.10.061.

(14) Elmekawy, A. A.; Sweeney, J. B.; Brown, D. R. Efficient Synthesis of Supported Proline Catalysts for Asymmetric Aldol Reactions. *Catalysis Science and Technology* **2015**, *5* (2), 690–696. https://doi.org/10.1039/c4cy00970c.

(15) Collier, V. E.; Ellebracht, N. C.; Lindy, G. I.; Moschetta, E. G.; Jones, C. W. Kinetic and Mechanistic Examination of Acid-Base Bifunctional Aminosilica Catalysts in Aldol and Nitroaldol Condensations. *ACS Catalysis* **2016**, *6* (1), 460–468. https://doi.org/10.1021/acscatal.5b02398.

(16) Bass, J. D.; Solovyov, A.; Pascall, A. J.; Katz, A. Acid-Base Bifunctional and Dielectric Outer-Sphere Effects in Heterogeneous Catalysis: A Comparative Investigation of Model Primary Amine Catalysts. *J Am Chem Soc* **2006**, *128* (11), 3737–3747.

(17) Pazdera, J.; Berger, E.; Lercher, J. A.; Jentys, A. Conversion of CO2 to Methanol over Bifunctional Basic-Metallic Catalysts. *Catalysis Communications* **2021**, *159*, 106347. https://doi.org/10.1016/J.CATCOM.2021.106347.

(18) Climent, M. J.; Corma, A.; Iborra, S. Conversion of Biomass Platform Molecules into Fuel Additives and Liquid Hydrocarbon Fuels. *Green Chemistry* **2014**, *16* (2), 516–547. https://doi.org/10.1039/C3GC41492B.

(19) Brunelli, N. A.; Jones, C. W. Tuning Acid–Base Cooperativity to Create next Generation Silica-Supported Organocatalysts. *Journal of Catalysis* **2013**, *308* (0), 60–72. https://doi.org/10.1016/j.jcat.2013.05.022.

(20) Brunelli, N. A.; Didas, S. A.; Venkatasubbaiah, K.; Jones, C. W. Tuning Cooperativity by Controlling the Linker Length of Silica-Supported Amines in Catalysis and CO2 Capture. *J Am Chem Soc* **2012**, *134* (34), 13950–13953. https://doi.org/10.1021/ja305601g.

(21) Abdelkrim, E. K.; El Kadib, A. Chitosan as a Sustainable Organocatalyst: A Concise Overview. *ChemSusChem* **2015**, *8* (2), 217–244. https://doi.org/10.1002/cssc.201402718.

(22) Khoury, C.; Gazit, O. M. Self-Organized Porous Titanium-Chitosan Hybrid Materials with Tunable Functions. *ChemNanoMat* **2018**, *4* (4), 353–360. https://doi.org/10.1002/cnma.201700358.

(23) Khoury, C.; Pappuru, S.; Gavriely, N.; Kleinerman, O.; Shpasser, D.; Segal-Peretz, T.; Gazit, O. M. Cooperatively Catalyzed Henry Reaction through Directed Metal-Chitosan Interactions. *ChemNanoMat* **2019**, *5* (12). https://doi.org/10.1002/cnma.201900431.

(24) Notestein, J. M.; Andrini, L. R.; Requejo, F. G.; Katz, A.; Iglesia, E. The Role of Outer-Sphere Surface Acidity in Alkene Epoxidation Catalyzed by Calixarene−Ti(IV) Complexes. *J Am Chem Soc* **2007**, *129* (50), 15585–15595. https://doi.org/10.1021/ja074614g.

(25) Moliner, M.; Román-Leshkov, Y.; Davis, M. E. Tin-Containing Zeolites Are Highly Active Catalysts for the Isomerization of Glucose in Water. *Proceedings of the National Academy of Sciences* **2010**, *107* (14), 6164–6168.

(26) Conrad, S.; Verel, R.; Hammond, C.; Wolf, P.; Göltl, F.; Hermans, I. Silica-Grafted SnIV Catalysts in Hydrogen-Transfer Reactions. *ChemCatChem* **2015**, *7* (20), 3270–3278. https://doi.org/10.1002/CCTC.201500630.

(27) Zaldivar, G. A. P.; Gushikem, Y.; Kubota, L. T. Tin(IV) Oxide Grafted on a Silica Gel Surface as a Conducting Substrate Base for Cupric Hexacyanoferrate. *Journal of Electroanalytical Chemistry and Interfacial Electrochemistry* **1991**, *318* (1–2), 247–254. https://doi.org/10.1016/0022-0728(91)85307-B.

(28) Musić, S.; Filipović-Vinceković, N.; Sekovanić, L. Precipitation of Amorphous SiO2 Particles and Their Properties. *Brazilian Journal of Chemical Engineering* **2011**, *28* (1), 89–94. https://doi.org/10.1590/S0104-66322011000100011.

(29) Thommes, M.; Kaneko, K.; Neimark, A. V.; Olivier, J. P.; Rodriguez-Reinoso, F.; Rouquerol, J.; Sing, K. S. W. Physisorption of Gases, with Special Reference to the Evaluation of Surface Area and Pore Size Distribution (IUPAC Technical Report). *Pure and Applied Chemistry* **2015**, *87* (9–10), 1051–1069. https://doi.org/10.1515/pac-2014-1117.

(30) Charlot, A.; Cuer, F.; Grandjean, A. The Effect of Pore Diameter in the Arrangement of Chelating Species Grafted onto Silica Surfaces with Application to Uranium Extraction. *New Journal of Chemistry* **2017**, *41* (2), 503–511. https://doi.org/10.1039/C6NJ03017C.

(31) Zhou, W.; Liu, Y.; Yang, Y.; Wu, P. Band Gap Engineering of SnO2 by Epitaxial Strain: Experimental and Theoretical Investigations. *Journal of Physical Chemistry C* **2014**, *118* (12), 6448–6453. https://doi.org/10.1021/jp500546r.

(32) Joshi, H.; Ochoa-Hernández, C.; Nürenberg, E.; Kang, L.; Wang, F. R.; Weidenthaler, C.; Schmidt, W.; Schüth, F. Insights into the Mechanochemical Synthesis of Sn-β: Solid-State Metal Incorporation in Beta Zeolite. *Microporous and Mesoporous Materials* **2020**, *309*, 110566. https://doi.org/10.1016/j.micromeso.2020.110566.

(33) Dijkmans, J.; Gabriëls, D.; Dusselier, M.; De Clippel, F.; Vanelderen, P.; Houthoofd, K.; Malfliet, A.; Pontikes, Y.; Sels, B. F. Productive Sugar Isomerization with Highly Active Sn in Dealuminated β Zeolites. *Green Chemistry* **2013**, *15* (10), 2777–2785. https://doi.org/10.1039/c3gc41239c.

(34) Astorino, E.; Peri, J. B.; Willey, R. J.; Busca, G. Spectroscopic Characterization of Silicalite-1 and Titanium Silicalite-1. *Journal of Catalysis* **1995**, *157* (2), 482–500. https://doi.org/10.1006/jcat.1995.1313.

(35) Dijkmans, J.; Dusselier, M.; Janssens, W.; Trekels, M.; Vantomme, A.; Breynaert, E.; Kirschhock, C.; Sels, B. F. An Inner-/Outer-Sphere Stabilized Sn Active Site in β-Zeolite: Spectroscopic Evidence and Kinetic Consequences. *ACS Catalysis* **2016**, *6* (1), 31–46. https://doi.org/10.1021/acscatal.5b01822.

(36) Sarr, B.; Diop, C. A. K.; Sidibé, M.; Rousselin, Y. Crystal Structure of Bis(Diisopropylammonium) Cis -Diiodidobis(Oxolato-K2 O1, O2)Stannate(IV). *Acta Crystallographica Section E: Crystallographic Communications* **2018**, *74* (Pt 4), 502–504. https://doi.org/10.1107/S2056989018003602.

(37) Teutsch, U.; Schmidtke, H. H. On the Problem of Assigning Electronic Transitions in Diketonate Complexes. Polarized Crystal Spectra of Tin(IV) and Antimony(V) Mono(Acetylacetonate) and -(Tropolonate) Complexes. *The Journal of Chemical Physics* **1986**, *84* (11), 6034–6047. https://doi.org/10.1063/1.450793.

(38) Tian, Q.; Zhuang, J.; Wang, J.; Xie, L.; Liu, P. Novel Photocatalyst, Bi 2Sn 2O 7, for Photooxidation of As(III) under Visible-Light Irradiation. *Applied Catalysis A: General* **2012**, *425–426*, 74–78. https://doi.org/10.1016/j.apcata.2012.03.005.

(39) Chiker, F.; Nogier, J. P.; Launay, F.; Bonardet, J. L. New Ti-SBA Mesoporous Solids Functionnalized under Gas Phase Conditions: Characterisation and Application to Selective Oxidation of Alkenes. *Applied Catalysis A: General* **2003**, *243* (2), 309–321. https://doi.org/10.1016/S0926-860X(02)00553-7.

(40) Majoul, N.; Aouida, S.; Bessaïs, B. Progress of Porous Silicon APTES-Functionalization by FTIR Investigations. *Applied Surface Science* **2015**, *331*, 388–391. https://doi.org/10.1016/j.apsusc.2015.01.107.

(41) White, L. D.; Tripp, C. P. Reaction of (3-Aminopropyl)Dimethylethoxysilane with Amine Catalysts on Silica Surfaces. *Journal of Colloid and Interface Science* **2000**, *232* (2), 400–407. https://doi.org/10.1006/jcis.2000.7224.

(42) Courtney, T. D.; Chang, C. C.; Gorte, R. J.; Lobo, R. F.; Fan, W.; Nikolakis, V. Effect of Water Treatment on Sn-BEA Zeolite: Origin of 960 Cm-1 FTIR Peak. *Microporous and Mesoporous Materials* **2015**, *210*, 69–76. https://doi.org/10.1016/j.micromeso.2015.02.012.

(43) Bell, J. V.; Heisler, J.; Tannenbaum, H.; Goldenson, J. Infrared Spectra of Metal Isopropoxides. *Analytical Chemistry* **1953**, *25* (11), 1720–1724. https://doi.org/10.1021/ac60083a034.

(44) Bradley, D. C.; Lewis, J.; Thomas, I. M. Et al. 2601 510. **1961**, 2601–2605.

(45) Lynch, C. T.; Mazdiyasni, K. S.; Smith, J. S.; Crawford, W. J. Infrared Spectra of Transition Metal Alkoxides. *Analytical Chemistry* **1964**, *36* (12), 2332–2337. https://doi.org/10.1021/ac60218a034.

(46) Kaya, M.; Baran, T.; Mentes, A.; Asaroglu, M.; Sezen, G.; Tozak, O. K. Extraction and Characterization of α -Chitin and Chitosan from Six Different Aquatic Invertebrates. *Food Biophysics* **2014**, *9*, 145–157. https://doi.org/10.1007/s11483-013-9327-y.

(47) Khan, A. S.; Khalid, H.; Sarfraz, Z.; Khan, M.; Iqbal, J.; Muhammad, N.; Fareed, M. A.; Rehman, I. U. Vibrational Spectroscopy of Selective Dental Restorative Materials. *Applied Spectroscopy Reviews* **2017**, *52* (6), 507–540. https://doi.org/10.1080/05704928.2016.1244069.

(48) Marchessault, R. H.; Pearson, F. G.; Liang, C. Y. Infrared Spectra of Crystalline Polysaccharides. *Biochimica et Biophysica Acta* **1960**, *45*, 499–507. https://doi.org/10.1016/0006-3002(60)91486-4.

(49) Morimoto, T.; Imai, J.; Nagao, M. Infrared Spectra of N-Butylamine Adsorbed Silica-Alumina. *The journal of Physical Chemistry* **1974**, *78*, 704–708.

(50) Turishchev, S. Y.; Chuvenkova, O. A.; Parinova, E. V.; Koyuda, D. A.; Chumakov, R. G.; Presselt, M.; Schleusener, A.; Sivakov, V. XPS Investigations of MOCVD Tin Oxide Thin Layers on Si Nanowires Array. *Results in Physics* **2018**, *11* (August), 507–509. https://doi.org/10.1016/j.rinp.2018.09.046.

(51) Jeong, M.; Yokoshima, T.; Nara, H.; Momma, T.; Osaka, T. Influence of the Diffusion-Layer Thickness during Electrodeposition on the Synthesis of Nano Core/Shell Sn-O-C Composite as an Anode of Lithium Secondary Batteries. *RSC Advances* **2014**, *4* (51), 26872–26880. https://doi.org/10.1039/c4ra03435j.

(52) Shircliff, R. A.; Stradins, P.; Moutinho, H.; Fennell, J.; Ghirardi, M. L.; Cowley, S. W.; Branz, H. M.; Martin, I. T. Angle-Resolved XPS Analysis and Characterization of Monolayer and Multilayer Silane Films for DNA Coupling to Silica. *Langmuir* **2013**, *29*, 4057. https://doi.org/10.1021/la304719y.

(53) Dong, W.; Li, H.; Xi, J.; Mu, J.; Huang, Y.; Ji, Z.; Wu, X. Reduced TiO2 Nanoflower Structured Photoanodes for Superior Photoelectrochemical Water Splitting. *Journal of Alloys and Compounds* **2017**, *724*, 280–286. https://doi.org/10.1016/j.jallcom.2017.06.246.

(54) Ma, J. W.; Lee, W. J.; Bae, J. M.; Jeong, K. S.; Oh, S. H.; Kim, J. H.; Kim, S. H.; Seo, J. H.; Ahn, J. P.; Kim, H.; Cho, M. H. Carrier Mobility Enhancement of Tensile Strained Si and SiGe Nanowires via Surface Defect Engineering. *Nano Letters* **2015**, *15* (11), 7204–7210. https://doi.org/10.1021/acs.nanolett.5b01634.

(55) Mania, P.; Verel, R.; Jenny, F.; Hammond, C.; Hermans, I. Thermal Restructuring of Silica-Grafted TiClx Species and Consequences for Epoxidation Catalysis. *Chemistry - A European Journal* **2013**, *19* (30), 9849–9858. https://doi.org/10.1002/chem.201300842.

(56) Min, H.; Girard-Lauriault, P. L.; Gross, T.; Lippitz, A.; Dietrich, P.; Unger, W. E. S. Ambient-Ageing Processes in Amine Self-Assembled Monolayers on Microarray Slides as Studied by ToF-SIMS with Principal Component Analysis, XPS, and NEXAFS Spectroscopy. *Analytical and Bioanalytical Chemistry* **2012**, *403* (2), 613–623. https://doi.org/10.1007/S00216-012-5862-5/FIGURES/8.

(57) Kulszewicz-Bajer, I.; Proń, A.; Abramowicz, J.; Jeandey, C.; Oddou, J. L.; Sobczak, J. W. Lewis Acid Doped Polyaniline: Preparation and Spectroscopic Characterization. *Chemistry of Materials* **1999**, *11* (3), 552–556. https://doi.org/10.1021/cm980727a.

(58) Maachou, H.; Genet, M. J.; Aliouche, D.; Dupont-Gillain, C. C.; Rouxhet, P. G. XPS Analysis of Chitosan–Hydroxyapatite Biomaterials: From Elements to Compounds. *Surface and Interface Analysis* **2013**, *45* (7), 1088–1097. https://doi.org/10.1002/SIA.5229.

(59) Farfan-Arribas, E.; Madix, R. J. Characterization of the Acid-Base Properties of the TiO2(110) Surface by Adsorption of Amines. *Journal of Physical Chemistry B* **2003**, *107* (14), 3225–3233. https://doi.org/10.1021/jp022344c.

(60) Head, A. R.; Chaudhary, S.; Olivieri, G.; Bournel, F.; Andersen, J. N.; Rochet, F.; Gallet, J. J.; Schnadt, J. Near Ambient Pressure X-Ray Photoelectron Spectroscopy Study of the Atomic Layer Deposition of TiO2 on RuO2(110). *Journal of Physical Chemistry C* **2016**, *120* (1), 243–251. https://doi.org/10.1021/acs.jpcc.5b08699.

(61) Sardo, M.; Afonso, R.; Juźków, J.; Pacheco, M.; Bordonhos, M.; Pinto, M. L.; Gomes, J. R. B.; Mafra, L. Unravelling Moisture-Induced CO2 Chemisorption Mechanisms in Amine-Modified Sorbents at the Molecular Scale. *Journal of Materials Chemistry A* **2021**, *9* (9), 5542–5555. https://doi.org/10.1039/D0TA09808F.

TOC graphics